Reduced transition strengths of low-lying yrast states in chromium isotopes in the vicinity of $N = 40$

Thomas Braunroth,[1,*] A. Dewald,[1] H. Iwasaki,[2] S. M. Lenzi,[3] M. Albers,[4] V. M. Bader,[2] T. Baugher,[2] T. Baumann,[5] D. Bazin,[5] J. S. Berryman,[5] C. Fransen,[1] A. Gade,[2] T. Ginter,[5] A. Gottardo,[6] M. Hackstein,[1] J. Jolie,[1] A. Lemasson,[7] J. Litzinger,[1] S. Lunardi,[3] T. Marchi,[8] V. Modamio,[8] C. Morse,[2] D. R. Napoli,[8] A. Nichols,[9] F. Recchia,[3] S. R. Stroberg,[2] R. Wadsworth,[9] D. Weisshaar,[5] K. Whitmore,[2] and K. Wimmer[10]

[1]*Institut für Kernphysik der Universität zu Köln, D-50937 Köln, Germany*

[2]*National Superconducting Cyclotron Laboratory and Department of Physics and Astronomy, Michigan State University, 640 South Shaw Lane, East Lansing, Michigan 48824-1321, USA*

[3]*Dipartimento di Fisica e Astronomia, Università di Padova and INFN Sezione di Padova, I-35131 Padova, Italy*

[4]*Physics Division, Argonne National Laboratory, Argonne, Illinois 60439, USA*

[5]*National Superconducting Cyclotron Laboratory, Michigan State University, East Lansing, Michigan 48824, USA*

[6]*Centre de Spectrométrie Nucléaire et de spectrométrie de Masse (CSNSM), CNRS/IN2P3 and Université Paris-Sud, F-91405 Orsay Campus, France*

[7]*GANIL, CEA/DSM-CNRS/IN2P3, F-14076 Caen Cedex 05, France*

[8]*INFN Laboratori Nazionali di Legnaro, I-35020 Legnaro (Padova), Italy*

[9]*Department of Physics, University of York, Heslington, York YO10 5DD, United Kingdom*

[10]*Department of Physics, University of Tokyo, Hongo, Bunkyo-ku, Tokyo 113-0033, Japan*

Background: In neutron-rich nuclei around $N = 40$ rapid changes in nuclear structure can be observed. While ^{68}Ni exhibits signatures of a doubly magic nucleus, experimental data along the isotopic chains in even more exotic Fe and Cr isotopes—such as excitation energies and transition strengths—suggest a sudden rise in collectivity toward $N = 40$.

Purpose: Reduced quadrupole transition strengths for low-lying transitions in neutron-rich ^{58,60,62}Cr are investigated. This gives quantitative new insights into the evolution of quadrupole collectivity in the neutron-rich region close to $N = 40$.

Method: The recoil distance Doppler-shift (RDDS) technique was applied to measure lifetimes of low-lying states in ^{58,60,62}Cr. The experiment was carried out at the National Superconducting Cyclotron Laboratory (NSCL) with the SeGA array in a plunger configuration coupled to the S800 magnetic spectrograph. The states of interest were populated by means of one-proton knockout reactions.

Results: Data reveal a rapid increase in quadrupole collectivity for ^{58,60,62}Cr toward $N = 40$ and point to stronger quadrupole deformations compared to neighboring Fe isotopes. The experimental $B(E2)$ values are reproduced well with state-of-the-art shell-model calculations using the LNPS effective interaction. A consideration of intrinsic quadrupole moments and B_{42} ratios suggest an evolution toward a rotational nature of the collective structures in ^{60,62}Cr. Compared to ^{58}Cr, experimental B_{42} and B_{62} values for ^{60}Cr are in better agreement with the $E(5)$ limit.

Conclusion: Our results indicate that collective excitations in neutron-rich Cr isotopes saturate at $N = 38$, which is in agreement with theoretical predictions. More detailed experimental data of excited structures and interband transitions are needed for a comprehensive understanding of quadrupole collectivity close to $N = 40$. This calls for additional measurements in neutron-rich Cr and neighboring Ti and Fe nuclei.

PACS number(s): 21.10.Tg, 23.20.−g, 25.60.−t, 27.40.+z

I. INTRODUCTION

With the ongoing progress in the field of experimental nuclear structure physics (e.g., via the development of new rare isotope beam facilities and state-of-the-art detector arrays), the frontier of experimentally accessible isotopes is pushed step by step toward the drip lines. This enables detailed studies of nuclear properties characterized by extreme isospin values and allows the systematic investigation of evolving nuclear structure along wide ranges of isotopic-isotonic chains.

Far away from the valley of β stability, experimental evidence for a variety of interesting phenomena has already been found. Prominent examples are the collapse of shell closures [1,2], the emergence of new pronounced shell gaps [3,4], shape coexistence [5], and widespread regions characterized by quickly and continuously evolving nuclear properties, e.g., the evolution of quadrupole collectivity in neutron-rich isotopes around $N = 40$.

It is often difficult to disentangle the influence of individual contributions of the nuclear force on the observed structural changes, but in some cases individual terms can be pointed out as the dominant driving force. Theoretical works by Otsuka *et al.* [6–8], for example, discuss the influence of the monopole component of the proton-neutron tensor force on the single-particle energies as a function of the neutron excess.

Nuclei in the region close to the neutron subshell closure at $N = 40$ and in the vicinity of $^{68}_{28}$Ni in particular are known for

*tbraunroth@ikp.uni-koeln.de

their rapidly evolving structural properties, which makes it a challenging region for theoretical descriptions.

So far, ^{80}Zr is the heaviest isotone with $N = 40$ for which information about excited states is known: The excitation energy of the first 2_1^+ state is only 289 keV and hints at a strong quadrupole deformation with $\beta_2 \approx 0.4$ [9]. With decreasing proton number, signatures for quadrupole collectivity are weakened toward proton magic ^{68}Ni, where both the high 2_1^+ state energy ($E(2_1^+) = 2033$ keV [10]) and the small reduced transition strength of $B(E2; 2_1^+ \rightarrow 0_1^+) = 51(12)\, e^2\text{fm}^4$ [11,12] indicate a subshell closure. However, the case of ^{68}Ni shows that one must be careful with the interpretation of such signatures: Although weak signs for an increased neutron shell gap were found, no pronounced shell closure was observed [13]. A study by Langanke *et al.* [14] concludes that a significant part of the experimental $B(E2)$ strength resides in excited states above 4 MeV, which questions the interpretation of the small experimental $B(E2)$ value as a good signature for a doubly magic character.

With the removal of protons from the $f_{7/2}$ orbital, the monopole tensor force between the $\pi f_{7/2}$ orbital and the $\nu f_{5/2}$ orbital becomes less attractive. This shifts the $\nu f_{5/2}$ orbital toward higher energies, which reduces the energy gap between the fp shell and the deformation driving $g_{9/2}$ orbital. This mechanism triggers a rapid development of collectivity and contributes to the onset of deformation in less proton-rich $_{24}$Cr and $_{26}$Fe nuclei toward $N = 40$. Along the $N = 40$ isotones, the excitation energies of the first 2_1^+ state in ^{66}Fe (573.4(1) keV [15]) and ^{64}Cr (420(7) keV [16]) decrease rapidly. In ^{68}Fe the trend of decreasing 2_1^+ state energies is continued ($E(2_1^+) = 521.2(1)$ keV [15]), while for ^{66}Cr no information about excited states has been reported yet.

In neutron-rich Fe isotopes, quadrupole deformation evolves rapidly from $N = 34$ to $N = 38$ and stays rather constant for more exotic ^{66,68}Fe$_{40,42}$ [17,18]. With two fewer protons, the neutron-rich Cr isotopes show a particularly rich variety of structural changes. While the local rise in the 2_1^+ state energy in ^{56}Cr$_{32}$ suggests a weak subshell closure at $N = 32$, experimental data toward $N = 40$ show a monotonic decrease of the 2_1^+ state energies [16,19–21] and increasing $B(E2; 2_1^+ \rightarrow 0_1^+)$ values [18,22,23]. The emerging picture of enhanced quadrupole collectivity is further reinforced by deduced deformation lengths in ^{60,62}Cr from proton inelastic scattering experiments [21].

Collectivity in Cr isotopes close to $N = 40$ has been studied with various theoretical approaches, ranging from shell-model calculations using different valence spaces and effective interactions [20,24–27] to various mean-field and beyond-mean-field calculations (see, for instance, Refs. [28–30]). By including the neutron $0g_{9/2}$ and $1d_{5/2}$ orbitals in the valence space, calculations within the spherical shell-model formalism using the LNPS interaction [27] are able to reproduce the rapidly evolving quadrupole collectivity in neutron-rich Fe and Cr isotopes. Shell-model calculations in a large model space using realistic interactions [31] and calculations with the proton-neutron version of the interacting boson model (IBM-2) were performed recently [32].

In general, the available experimental information in neutron-rich Cr isotopes with $A \geqslant 58$ is sparse. While level

TABLE I. A1900 settings and properties of the secondary ^{A}Mn beams as measured with the S800.

A	PT d in μm	Wedge d in μm	$\Delta p/p$ (%)	Energy (AMeV)	Intensity (pps)	Purity (%)
^{59}Mn	352	390	1.0	92.1	$1.8 \cdot 10^5$	67
^{61}Mn	540	240	1.5	91.9	$1.8 \cdot 10^4$	62
^{63}Mn	517	180	2.0	98.0	$3.1 \cdot 10^3$	25

schemes were investigated in some detail, $B(E2)$ values are only known for the $2_1^+ \rightarrow 0_1^+$ transitions up to $N = 40$. Experimental quadrupole transition strengths between higher-lying excited states are important to gain insights into the nature of the observed quadrupole collectivity and will contribute to a more comprehensive understanding of shell evolution in nuclei far away from the valley of β stability.

From a general point of view, the atomic nucleus is subject to quantal phase transitions [33,34] when changing its numbers of protons and neutrons. Between $N = 32$ and $N = 40$, experimental and theoretical information support the picture of changing shape phases in the Cr isotopes. With increasing neutron excess, band-mixing calculations indicate a gradual replacement of the spherical shapes for low-lying yrast states with coexisting deformed structures associated with a well-deformed rotational band built on a neutron $(g_{9/2})^2$ configuration [35]. Toward $N = 40$, the almost spherical shape of ^{56}Cr$_{32}$ is replaced by a stable deformation, which motivates the search for critical-point nuclei in this potentially phase transitional region. In fact, Mărginean *et al.* [36] realized that the ratios between excitation energies for low-lying states in ^{58}Cr are close to the theoretical values predicted for an $E(5)$ nucleus [37]. An additional fingerprint of the $E(5)$ symmetry must come from the ratios between $B(E2)$ values which were unknown prior to this work.

II. EXPERIMENTAL SETUP

The experiment was performed at the National Superconducting Cyclotron Laboratory (NSCL) at Michigan State University. The Coupled Cyclotron Facility [38] provided a ^{82}Se primary beam with an energy of 140 AMeV and an intensity of 35 pnA on average.

At the entrance of the fragment separator A1900 [39] the primary beam was fragmented on ^{9}Be production targets (PT) with thicknesses d of 352, 540, and 517 mg/cm^2 to produce secondary beams of ^{59,61,63}Mn, respectively. The A1900 separated the produced beam cocktail, selecting the desired Mn isotopes on the basis of their rigidity. The suppression of unrequested particles was improved by a wedge-shaped Al degrader located between the two dipole pairs of A1900. Momentum acceptances $\Delta p/p$ for each beam setting and the resultant average beam rates as detected with the S800 spectrograph [40] are summarized in Table I.

The constituents of the secondary beam were identified by a time-of-flight measurement between the focal plane of A1900 and the object point of the S800 spectrograph beam line. The secondary beams of interest with mean

TABLE II. Plunger setup and mean recoil velocities. See text for details.

A	Be target d in μm	Au degrader d in μm	$\overline{\beta}_0$ (%)	$\overline{\beta}_T$ (%)	$\overline{\beta}_D$ (%)
^{58}Cr	287.2	254.5	41.5	40.7	36.1
^{60}Cr	520.1	254.5	41.4	40.2	35.5
^{62}Cr	1294.5	254.5	42.6	39.7	35.0

velocity $\overline{\beta}_0$ (relative to the speed of light) impinged on a ^{9}Be plunger target, in which excited states in ^{58,60,62}Cr were mainly populated by one-proton knockout reactions. Recoils left the target with a velocity $\overline{\beta}_T$, before they were slowed down to $\overline{\beta}_D$ by a gold degrader, which was placed at a well-defined target-to-degrader separation Δd. This led to two regimes characterized by distinct recoil velocities, allowing the application of the RDDS technique [41]. Typical values for Δd were adjusted in the range between several micrometers and several millimeters. Further downstream a thin polyester film was mounted, which significantly reduced the number of Mn isotopes in charge state 24^+ by electron stripping. The target and degrader foils were mounted and aligned in the housing of the differential plunger device TRIPLEX (triple plunger for exotic beams) [42], which was also used in recent lifetime experiments at NSCL [43,44]. Details about the foil configurations and the observed recoil velocities are summarized in Table II. Information about target-to-degrader separations Δd for each of the studied Cr isotopes is given in the following section.

Projectile-like recoils entering the S800 were identified unambiguously by the S800 detector system [45]: The 16-fold ionization chamber measured the energy loss ΔE, while two scintillators measured the time of flight between the object scintillator of the S800 analysis line and the focal plane scintillator of the S800 spectrograph. The S800 focal plane detector system is completed by a pair of position-sensitive cathode readout-drift counters [46], which allowed the identification of the recoil velocity vector.

Prompt γ rays were detected with the SeGA array [47] in its plunger configuration, which consisted of 15 32-fold segmented HPGe detectors. The detectors were arranged in two rings with eight (seven) detectors placed upstream (downstream) of the plunger degrader at a distance of 24 (29) cm with respect to the degrader foil. The average angle between upstream (us) / downstream (ds) detector ring and beam axis was given by $\theta_{us} \approx 140°$ and $\theta_{ds} \approx 30°$.

III. DATA ANALYSIS AND RESULTS

The particle identification was achieved on an event-by-event basis with the S800 detector system. Using trajectory reconstruction [48], the recoil velocity vector $\vec{v}_r$ at the degrader position is reconstructed (assuming that scattering within the stripper foil may be neglected). This was used to calculate the effective polar angle θ_{S800} between $\vec{v}_r$ and $\vec{r}_{SeGA}^{max}$, the latter being the position vector of the SeGA segment with the largest γ-ray energy deposition. Combined with the recoil velocity β_{S800} as measured with the S800, it allows a Doppler correction of the
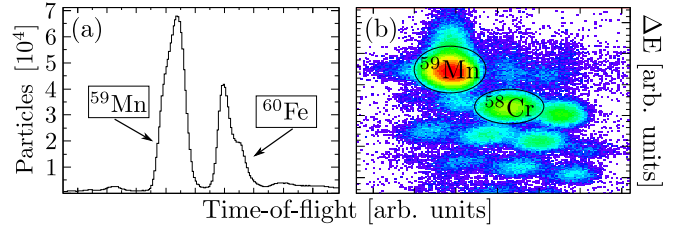

FIG. 1. (Color online) Particle identification for the ^{58}Cr setting. (a) Particles of the secondary beams are identified by means of a time-of-flight measurement. (b) Reacted beam particles are identified by their energy loss ΔE in the ionization chamber and their time-of-flight through S800 (incoming particle gate is set on ^{59}Mn).

measured energies E_{lab} event by event according to

$$E_0 = E_{lab} \frac{1 - \beta_{S800} \cos \theta_{S800}}{\sqrt{1 - \beta_{S800}^2}}. \tag{1}$$

Due to the chosen momentum acceptance of the secondary beam (see time-of-flight distribution in Fig. 1) and the thick foil configuration, the width of the velocity distribution for recoils is typically between 2 and 5 % and therefore not negligible. Combined with the low statistics of the experiment and the fact that data for only a few target-to-degrader separations were collected, an application of the differential decay-curve method [41] is not recommended. Therefore, absolute distance information is necessary. Mean-zero offsets Δx_0 were evaluated by linear extrapolation of the capacitance signal between target and degrader [49].

The number of (undesired) degrader excitation was determined using runs at large target-to-degrader separations, for which the flight time of the recoils exceeded the expected level lifetime significantly. Hence, γ events assigned to the degrader peak are accounted as degrader excitation.

Lifetimes are determined with a dedicated Monte Carlo simulation tool [50,51] based on ROOT [52] and the GEANT4 TOOLKIT [53]. In this simulation, input parameters for basic beam properties (e.g., isotope, beam energy, momentum distribution), foil properties (e.g., material, thickness) and characteristics of the reaction mechanism are deduced from experimental observables. The geometry information of the SeGA detectors was measured precisely with a laser tracking system and was incorporated into the simulation. The target-to-degrader separations were measured with the linear encoder implemented in the plunger motor.

The validity of the simulation was checked by γ-efficiency measurements. Data with a ^{152}Eu source was taken for different source positions (e.g., between target and degrader and downstream of the degrader). The simulation could reproduce the relative efficiency of both rings of the SeGA array satisfactory with relative errors smaller than 7% in the energy range from 344 to 1408 keV. Since the simulation cannot reproduce adequately the complete γ background (e.g., from the unaccounted interaction of beam with matter), an empirical description was necessary and was added to the simulated spectra. In the energy range of interest, the continuous background was modeled with a combination of two linear functions.

Within the simulation, lifetimes were varied in discrete steps and for each assumed lifetime a χ^2 was calculated according to

$$\chi^2 = \sum_{\Delta d} \sum_{ds,us} \sum_i \left(\frac{I_{exp}(i) - I_{sim}(i)}{\Delta I_{exp}(i)} \right)^2, \qquad (2)$$

where $I_{exp}(i)$ ($I_{sim}(i)$) is the intensity of the experimental (simulated) spectrum in bin i. In order to increase the sensitivity of the method to lifetime effects, only bins i close to the centroids of the amplitudes were taken into account, which corresponds to a considered energy range of roughly ± 10 keV around the amplitudes. The binning was chosen such that (a) the amplitudes of the target and degrader components were clearly identifiable and distinguishable and (b) the influences of statistical artifacts in the experimental data were minimized. Under these conditions the extracted lifetimes were robust to modified binnings. A binning of 4 keV/bin was usually sufficient but in some cases the binning was increased to 8 keV/bin to analyze transitions with low statistics reasonably. The sum is taken over both detector rings and all target-to-degrader separations Δd. See Sec. III E for the treatment of errors in the analysis.

A. ^{58}Cr

Mărginean *et al.* [36] observed excited states in ^{58}Cr up to the 8_1^+ state. A more detailed investigation of the level scheme of ^{58}Cr, including nonyrast levels, was performed by Zhu *et al.* [19].

Experimental data with the ^{9}Be plunger target but without the Au degrader (*target-only data*) were collected over 5.5 h, where sufficient statistics was collected to clearly identify transitions with centroidal energies of 881(1), 1058(1), 1282(2), and 1374(3) keV. Within the simulation, relative γ intensities of 100, 60.7, 10.8, and 8.6%, respectively, were found best to reproduce the experimental spectra.

According to Ref. [19], these energies can be assigned to the transitions $2_1^+ \rightarrow 0_1^+$ (881 keV), $4_1^+ \rightarrow 2_1^+$ (1058 keV), $6_1^+ \rightarrow 4_1^+$ (1282 keV), and $5_1^- \rightarrow 4_1^+$ (1374 keV).

Weak signs for peaks at 950(3) and 1100(3) keV are visible with relative intensities of 3(1) and 4(1)%, respectively. These peaks cannot be clearly associated with γ transitions in ^{58}Cr. Hence, they are not placed in the level scheme. The Doppler-shift-corrected target-only spectrum for all detectors in combination with the best simulation is shown in Fig. 2. To extract lifetime information, plunger data for five nominative target-to-degrader separations (0, 25, 50, 500, and 4000 μm) were collected over a total of 15 h. The mean-zero offset Δx_0 was determined to 21 μm.

Since the expected lifetimes for the states of interest are below 10 ps, the target-to-degrader separation at 4000 μm was used to quantify the contribution of degrader excitation. No feeding transitions could be observed for the 6_1^+ and 5_1^- states. In the analysis prompt feeding is therefore assumed for these states. Since these states were only populated weakly, data for short distances ($d = 0$, 25, and 50 μm) were summed up to gain enough statistics for a lifetime analysis. Still, statistics were so low that only the downstream detector ring
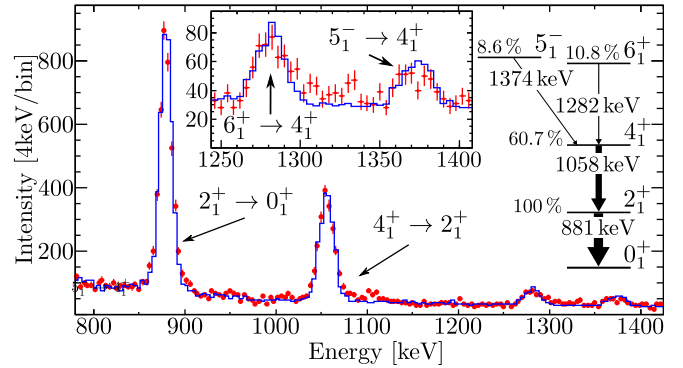

FIG. 2. (Color online) ^{58}Cr, target-only γ-ray spectrum. The Doppler-shift-corrected experimental data for all detectors is shown in red (light gray; with errors), while the simulation is shown with a solid blue (dark gray) line. The feeding scheme as used in the simulation is depicted on the right side.

at $\theta \approx 30°$ was used in the lifetime analysis. For the 6_1^+ state, the present separations cover the sensitive region and the analysis led to a lifetime of $1.0^{+0.7}_{-0.5}$ ps. The 5_1^- state appears to have a much longer lifetime. The short separations are therefore unsuited to determine the lifetime precisely and, as a consequence, only a lower limit of 7 ps can be given. The corresponding spectrum is shown in Fig. 3. For the 4_1^+ state feeding transitions from the 6_1^+ and 5_1^- states were taken into account according to the feeding scheme. Besides the short separations, the target-to-degrader separation at 500 μm is within the sensitive region. Best results were achieved for a level lifetime of $\tau(4_1^+) = 2.8(4)$ ps. The error includes all uncertainties as discussed later in Sec. III E.

Similarly, the lifetime of the 2_1^+ state is deduced to be 6.8(9) ps. A comparison between experimental data and best simulations for all distances and both SeGA rings is depicted in Fig. 4.

B. ^{60}Cr

For ^{60}Cr, target-only data were collected over 2.5 h and transitions with centroids at 643(3), 818(3), and 984(4) keV

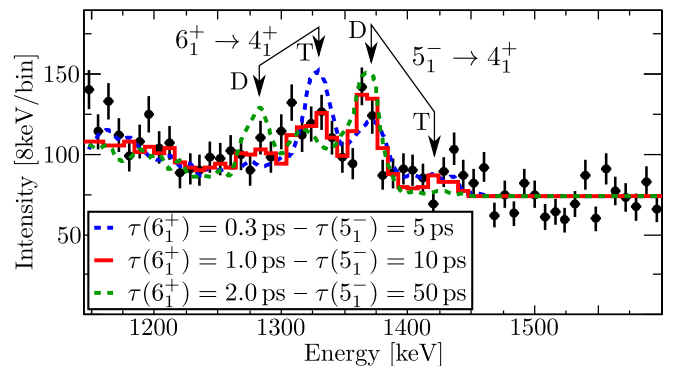FIG. 3. (Color online) ^{58}Cr, lifetime of the 6_1^+ and 5_1^- states. The experimental spectrum (black dots with error bars) and the best simulated spectrum (red [light gray] solid line) are shown for the detector ring at $\theta \approx 30°$. Here, T (D) denotes the decay component behind the target (degrader).

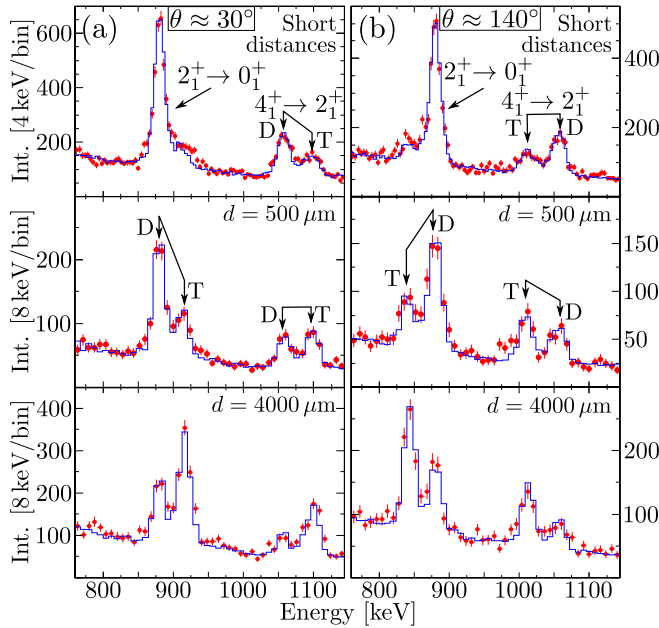FIG. 4. (Color online) ^{58}Cr, plunger data. Comparison of experimental data (red [light gray] dots with error bars) and best simulation with $\tau(2_1^+) = 6.8$ ps and $\tau(4_1^+) = 2.8$ ps (blue [dark gray] solid line) for (a) detectors at $\theta \approx 30°$ and (b) detectors at $\theta \approx 140°$. The spectra denoted with "short distances" are the sum of 0,25, and 50 μm.

were identified. The simulation tool reproduces the experimental spectra with corresponding relative intensities of 100, 54.6, and 18.2%, respectively. The energies are in good agreement with the lowest yrast transitions as measured by Zhu *etal.* [19], who used deep inelastic and fusion evaporation reactions to investigate low-lying states up to $I^\pi = 10^+$. Besides these yrast transitions, no further transitions are visible. The Doppler-shift-corrected target-only spectrum for all detectors and the best simulation are shown in Fig. 5.

Plunger data for four target-to-degrader separations (150, 300, 450, and 4000 μm) were collected over a total of 29 h. Due to the short lifetime of the 4_1^+ state, the largest separation allows us to quantify the contribution of degrader excitation, which—after scaling for the different target thicknesses—is in
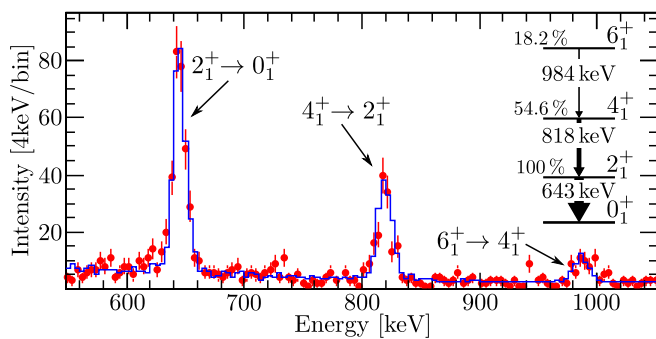

FIG. 5. (Color online) ^{60}Cr, target-only γ-ray spectrum. The experimental data (red [light gray] dots with errors) and the best simulation (blue [dark gray] solid line) are shown for the statistics of all detectors. The feeding scheme as used in the simulation is depicted on the right side.
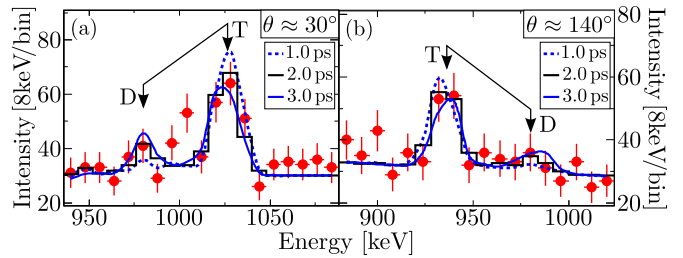

FIG. 6. (Color online) ^{60}Cr, lifetime of the 6_1^+ state. The experimental spectrum (red [light gray] dots with errors) and the best simulation for a lifetime of 2 ps (black solid line) are shown for (a) detectors at $\theta \approx 30°$ and (b) detectors at $\theta \approx 140°$.

good agreement with the corresponding target-degrader yield ratio from the ^{58}Cr experiment. The mean-zero offset Δx_0 was evaluated to 34 μm.

To determine the lifetime of the 6_1^+ state it was necessary to sum up the data for 150, 300, and 450 μm to compensate for low statistics. The χ^2 is minimized for a lifetime of 2(1) ps. The associated experimental and simulated spectra are shown in Fig. 6. In the analysis of the lifetime for the 4_1^+ state, the target-to-degrader separations of 150, 300, and 450 μm are within the sensitive region. The agreement between experiment and simulation is best for a lifetime of $\tau(4_1^+) = 5.2(9)$ ps.

The target-to-degrader separation at 4000 μm is most helpful for the lifetime analysis of the 2_1^+ state and the smallest χ^2 is found for $\tau(2_1^+) = 26.5(32)$ ps.

A comparison between experimental spectra and best simulations is depicted in Fig. 7 for both detector rings and all target-to-degrader separations.

C. ^{62}Cr

Sorlin *et al.* [20] proposed a candidate for $2_1^+ \to 0_1^+$ transition in ^{62}Cr at 446(1) keV, which was later confirmed by Aoi *et al.* (449(4) keV) [21] and Gade *et al.* (440(7) keV) [16]. In Ref. [21] a transition at 734(10) keV was observed for the first time and tentatively assigned to the $4_1^+ \to 2_1^+$ transition. Gade and colleagues confirmed this transition with a measurement of 725(9) keV. So far, no further transitions are known in ^{62}Cr.

Due to the low intensity of the secondary beam we concentrated on collecting plunger data. The level scheme was deduced from summed γ-ray spectra, in which only the lowest yrast transitions at 445(2) keV $(2_1^+ \to 0_1^+)$ and 728(3) keV $(4_1^+ \to 2_1^+)$ with relative intensities of 100 % $(2_1^+ \to 0_1^+)$ and 65 % $(4_1^+ \to 2_1^+)$ were identified unambiguously.

Plunger data were collected for two target-to-degrader separations of 0 μm (72 h) and 7000 μm (23 h), where the small (large) separation sheds light on the lifetime of the 4_1^+ (2_1^+) state. The mean-zero offset Δx_0 was evaluated to 26 μm. The χ^2 is minimized for lifetimes of 6.8(8) ps $(4_1^+$ state), and 125(13) ps $(2_1^+$ state). The best simulations and the experimental spectra are depicted in Fig. 8.

D. Analysis of the decay curves

In addition to a lifetime analysis based on Monte Carlo simulations, a conventional analysis of the underlying decay
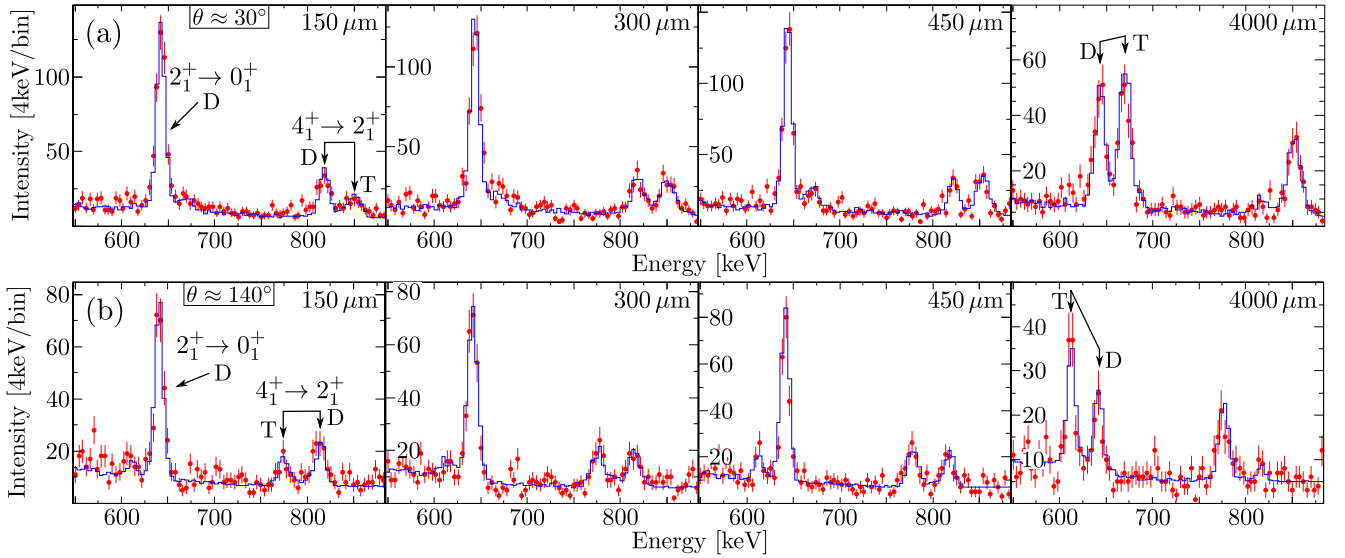
FIG. 7. (Color online) ^{60}Cr, plunger data. Comparison of experimental data (red [light gray] dots with error bars) and best simulation with $\tau(2_1^+) = 26.5$ ps and $\tau(4_1^+) = 5.2$ ps (blue [dark gray] solid line) for (a) detectors at $\theta \approx 30°$ and (b) detectors at $\theta \approx 140°$.

curves was conducted for cross-checking purposes. Compared to standard plunger experiments with small recoil velocities and almost negligible foil thicknesses, a few assumptions are necessary:

1. The effective target-to-degrader separation Δd_{eff} is given by the sum of the nominal separation Δd, the mean-zero offset Δx_0 and—for target and degrader—half the foil thicknesses Δ_T, Δ_D:

$$\Delta d_{\text{eff}} = \Delta d + \Delta x_0 + 0.5(\Delta_T + \Delta_D).$$

2. It is assumed that the recoils move with a velocity which is equivalent to the mean recoil velocity $\overline{\beta}_T$ as measured
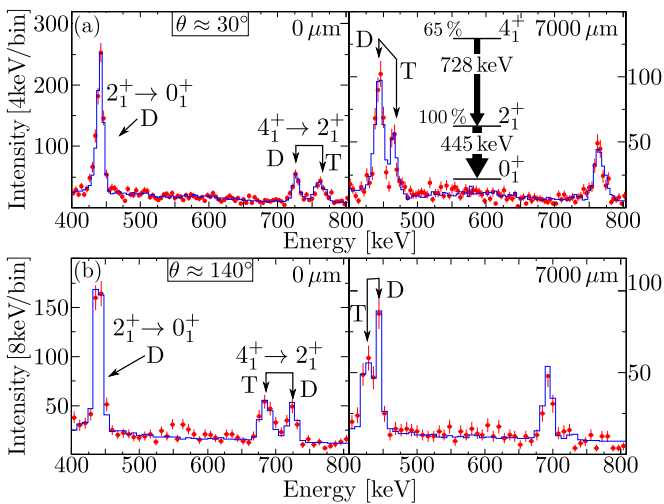

FIG. 8. (Color online) ^{62}Cr, plunger data. Comparison of experimental data (red [light gray] dots with error bars) and best simulation with $\tau(2_1^+) = 125$ ps and $\tau(4_1^+) = 6.8$ ps (blue [dark gray] solid line) for (a) detectors at $\theta \approx 30°$ and (b) detectors at $\theta \approx 140°$. In the simulation a level scheme as depicted in the upper right spectrum is assumed.

with the S800 in the target-only runs (^{58,60}Cr) or estimated in the plunger run (^{62}Cr). This recoil velocity was also used to compute the Lorentz-contracted $\Delta\tilde{d}_{\text{eff}}$ and the corresponding flight time.

3. The intensities for target (I_T) and degrader (I_D) are evaluated by correcting for the efficiency differences as measured with the ^{152}Eu source.

4. For ^{58,60}Cr, the contribution of degrader excitation is quantified with the largest separation. Due to the lack of statistics a scaled value with respect to the ^{58}Cr setup was taken for ^{62}Cr which accounts for the different target thicknesses.

5. With respect to the excitation energies, lifetimes are determined from higher-lying states to lower-lying states with an analytic expression for $I_D/(I_T + I_D)$ where the observed feeding is taken into account.

The decay curves for the 4_1^+ state and the 2_1^+ state in ^{58,60,62}Cr are depicted in Fig. 9. It is worthwhile to note that within the errors the deduced lifetimes are in agreement with the results stemming from the more sophisticated Monte Carlo simulations. The latter will be adopted in the following discussion.

E. Error estimations

Lifetimes were determined by the least squares method and the results are summarized in Table V. The quoted errors include statistical uncertainties as well as ambiguities from the degrader excitation contribution and feeding effects. Each contribution is listed in Table III and added in quadrature for the final error. Detailed procedures are described in the following.

First, we evaluate the statistical error directly related to the yield of the transition of interest. Within an experimental spectrum a transition is distributed over several bins i where each bin contains N_i events. Hence, from a statistical point of view and according to the maximum likelihood method, we can modify the experimental spectrum by randomly

TABLE III. Investigation of statistical errors introduced by model parameters and their influence on the measured lifetimes in ^{58,60,62}Cr.

J_i^π	Parameter p_i	^{58}Cr				^{60}Cr				^{62}Cr			
		$\langle p_i \rangle$	$\frac{\partial \tau [\mathrm{ps}]}{\partial p_i}$	Δp_i	$\frac{\partial \tau}{\partial p_i}\Delta p_i$	$\langle p_i \rangle$	$\frac{\partial \tau [\mathrm{ps}]}{\partial p_i}$	Δp_i	$\frac{\partial \tau}{\partial p_i}\Delta p_i$	$\langle p_i \rangle$	$\frac{\partial \tau [\mathrm{ps}]}{\partial p_i}$	Δp_i	$\frac{\partial \tau}{\partial p_i}\Delta p_i$
4_1^+	Zero offset Δx_0 (μm)	21	0.008	10	0.08	34	0.008	10	0.08	26	0.009	20	0.18
	Recoil velocity β_T	40.73	-0.090	0.1	0.01	40.18	-0.173	0.1	0.02	39.45	-0.198	0.1	0.02
	Degrader excitation (%)	33.0	-0.083	2.0	0.17	18.0	-0.119	3.0	0.36	7.0	-0.127	3.0	0.38
	Lifetime τ_{6^+} (ps)	1.0	-0.130	$^{+0.7}_{-0.5}$	$^{+0.07}_{-0.09}$	2.0	-0.421	1.0	0.42				
	Feeding from 6^+ state (%)	10.8	-0.014	3.0	0.04	18.2	-0.026	3.0	0.08				
	Lifetime τ_{5^-} (ps)	7		$^{+200}_{-0}$	$^{+0}_{-0.13}$								
	Feeding from 5^- state (%)	8.6	-0.045	3.0	0.14								
2_1^+	Zero offset Δx_0 (μm)	21	0.017	10	0.17	34	0.009	10	0.09	26	0.018	20	0.36
	Recoil velocity β_T	40.73	-0.276	0.1	0.03	40.18	-0.864	0.1	0.09	39.45	-3.91	0.1	0.39
	Degrader excitation (%)	33.0	-0.134	2.0	0.27	18.0	-0.595	3.0	1.79	7.0	-1.77	3.0	5.31
	Lifetime τ_{4^+} (ps)	2.8	-0.76	$^{+0.38}_{-0.42}$	$^{+0.32}_{-0.29}$	5.2	-0.676	0.85	0.54	6.8	-1.66	0.75	1.25
	Feeding from 4^+ state (%)	60.7	-0.065	1.0	0.07	54.6	-0.065	3.0	0.20	65	-0.160	3.0	0.48

varying the number of events in bin i following the Poisson distribution. Within this modified γ spectrum the total peak intensity of a γ transition (distributed on several bins) is expected to deviate from the total peak intensity as seen in the original experimental spectrum. Applied to plunger data, both peaks are affected and the influence of these variations on the deduced lifetime τ can be related to the experimental uncertainty due to the Poisson statistics. For the error analysis, $n = 10^4$ modified spectra are generated in which variations affect only the investigated transition. Each modified spectrum is then compared to sets of simulated spectra in which different lifetimes are assumed. For each comparison the χ^2 is calculated according to Eq. (2) and scanned for the best fitting lifetime assumption. A histogram
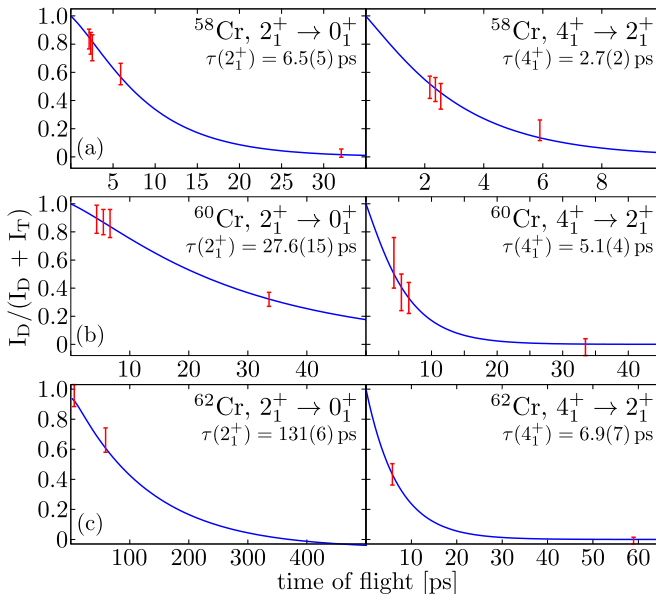

FIG. 9. (Color online) Lifetimes of the 2_1^+ and 4_1^+ states in (a) ^{58}Cr, (b) ^{60}Cr, and (c) ^{62}Cr as deduced from the decay curves. The experimental data are depicted in red (light gray) and the fitted decay curves are depicted in blue (dark gray). See text for further details.

is then filled with the frequency of the best fitting lifetime, which is then fitted with a Gaussian function whose standard deviation is a measure solely for the statistical uncertainty $\Delta\tau_t$ of the deduced lifetime (see Fig. 10) related to the transition of interest. Next, we consider additional ambiguities due to the degrader excitation and feeding effects. The present analysis is based on a Monte Carlo simulation, whose input parameters p_i are derived from experimental observables. Prominent examples for such parameters are given by the contribution of degrader excitation and the uncertainties in the observable feeding-scheme. Due to the linear extrapolation of the capacitance signal and inhomogeneous foil surfaces, the zero offsets and, hence, the target-to-degrader separations, are known with only a limited precision. This error is estimated to be 10 μm.

Here, we want to disentangle such effects from the statistical error and consider their influences on the lifetime separately and independent from each other. For this purpose, we vary within the simulation the parameters p_i in discrete steps around $\langle p_i \rangle$. For each varied parameter p_i, the modified spectra are compared to sets of simulations with different lifetime assumptions. Similar to the above mentioned procedure, the
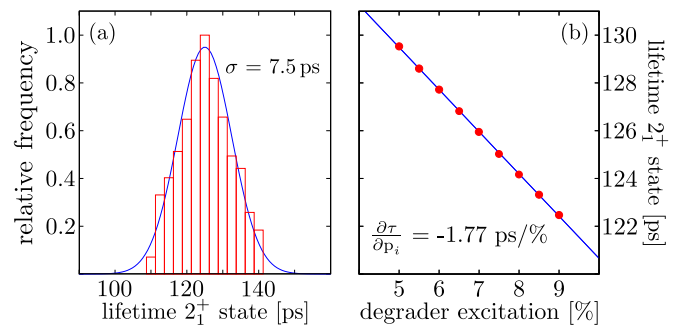

FIG. 10. (Color online) The error analysis applied to the $2_1^+ \rightarrow 0_1^+$ transition in ^{62}Cr. (a) Analysis of the statistical error $\Delta\tau_t$. (b) Influence of degrader excitation on the deduced lifetime. Simulated data is shown in red (light gray) while fits are shown in blue (dark gray).

TABLE IV. Statistical errors directly related to the transitions of interest ($\Delta\tau_t$) and errors related to ambiguities in the model parameters ($\Delta\tau_m$) for the 2_1^+ state and 4_1^+ state in ^{58,60,62}Cr. See text for details.

$^A X$	J_1^π	τ (ps)	$\Delta\tau_t$ (ps)	$\Delta\tau_m$ (ps)
^{58}Cr	2_1^+	6.80	0.43	$^{+0.46}_{-0.44}$
	4_1^+	2.80	0.14	$^{+0.24}_{-0.28}$
^{60}Cr	2_1^+	26.5	1.3	1.9
	4_1^+	5.20	0.29	0.56
^{62}Cr	2_1^+	125.0	7.5	5.5
	4_1^+	6.80	0.34	0.42

resulting distribution is fitted with a Gaussian function and for each p_i value the mean lifetime is computed. In first order a linear relationship between the deduced mean lifetime τ and p_i can be observed, giving access to the partial derivative $\frac{\partial\tau}{\partial p_i}$ (see Fig. 10). The uncertainty Δp_i for parameter p_i is either given directly by experimental uncertainties or has to be estimated. The variance is the sum of all considered statistical variances and the final error is calculated according to

$$\Delta\tau = \sqrt{(\Delta\tau_t)^2 + \sum_i \left(\frac{\partial\tau}{\partial p_i}\Delta p_i\right)^2} \qquad (3)$$

All considered parameters p_i, their uncertainties Δp_i, and the corresponding partial derivative $\frac{\partial\tau}{\partial p_i}$ are summarized in Table III. From these results, we conclude that—next to the influence of feeding properties—the uncertainty of degrader excitation contributes significantly to the final error. The error related to the yield of the transition of interest, $\Delta\tau_t$, and the error related to ambiguities in the model parameters, $\Delta\tau_m$, are listed in Table IV.

IV. DISCUSSION

The results of the experiment are summarized in Table V. The quoted errors for the lifetime τ incorporate all errors as discussed in Sec. III E. When neglecting the influence of internal conversions, reduced quadrupole transition strengths $B(E2;\downarrow)$ are derived from the transition energy E_γ and the measured lifetimes τ according to

$$B(E2;\downarrow)\,[e^2\text{fm}^4] = \frac{1}{1.22\times10^9}\frac{1}{E_\gamma[\text{MeV}]^5}\frac{1}{\tau[\text{s}]}. \qquad (4)$$

We assume that the error of the lifetime τ and the transition energy E_γ follow a normal distribution. A Monte Carlo simulation with 10^6 iterations was used to calculate $B(E2)$ values according to Eq. (4). The median of the hereby generated distribution corresponds to the adopted $B(E2)$ value, while the associated errors correspond to quantiles $q(16\%)$ and $q(84\%)$, respectively. The values are compared to former experimental results taken from Coulomb excitation experiments at intermediate energies [23,54]. In addition, the results are compared to calculations performed with the shell model using the LNPS interaction [27] and the proton-neutron version of the interacting boson model (IBM-2) [32].

The present $B(E2;2_1^+\to0_1^+)$ values in ^{58,60,62}Cr are in agreement with previous results [23,54]. The only exception is given by ^{58}Cr, for which the $B(E2;2_1^+\to0_1^+)$ value as published by Baugher *et al.* is slightly below our result. The present $B(E2;2_1^+\to0_1^+)$ values suggest that the increase in quadrupole collectivity is even more rapid than inferred from the results of Baugher and coworkers.

For higher-lying transitions no experimental $B(E2)$ values were known prior to this work. In ^{58}Cr, the $B(E2;4_1^+\to2_1^+)$ and $B(E2;2_1^+\to0_1^+)$ values are similar. For ^{60}Cr and ^{62}Cr, the $B(E2;4_1^+\to2_1^+)$ values are significantly larger than the corresponding $B(E2;2_1^+\to0_1^+)$ values. The significance of the deduced $B(E2;6_1^+\to4_1^+)$ values in ^{58,60}Cr suffers from the small statistics. In ^{58}Cr it appears comparable to the $B(E2)$ values of the lower yrast transitions and in ^{60}Cr

TABLE V. Summary of the experimental results. Values marked with * are related to effective lifetimes, where feeding contributions are not taken into account in the analysis. The experimental results are compared to previous results from Coulomb excitation experiments at intermediate energies, IBM-2 calculations [32], and shell-model calculations using the LNPS interaction [27]. See text for further details.

A	$J_i \to J_f$	E_γ (keV)	Experiment		Previous works $B(E2;\downarrow)$ (e^2fm^4)	Theory	
			This work			IBM-2 $B(E2;\downarrow)$ (e^2fm^4)	LNPS $B(E2;\downarrow)$ (e^2fm^4)
			$\tau(J_i)$ (ps)	$B(E2;\downarrow)$ (e^2fm^4)			
^{58}Cr	$2_1^+ \to 0_1^+$	880.7(2) [19]	6.8(9)	227^{+35}_{-26}	172(25) [23], 197(36) [54]	228	184
	$4_1^+ \to 2_1^+$	1057.9(3) [19]	2.8(4)	221^{+36}_{-28}		327	227
	$6_1^+ \to 4_1^+$	1280.5(3) [19]	$1.0^{+0.7*}_{-0.5}$	228^{+199*}_{-94}		339	191
	$5_1^- \to 4_1^+$	1372.5(3) [19]	$> 7^*$				
^{60}Cr	$2_1^+ \to 0_1^+$	643.9(2) [19]	26.5(32)	279^{+38}_{-30}	276(29) [23]	266	262
	$4_1^+ \to 2_1^+$	816.8(4) [19]	5.2(9)	433^{+90}_{-64}		388	372
	$6_1^+ \to 4_1^+$	985.3(2) [19]	$2(1)^*$	426^{+355*}_{-142}		418	374
^{62}Cr	$2_1^+ \to 0_1^+$	446(1)[20]	125(13)	371^{+43}_{-35}	321^{+60}_{-49}, 325(44) [23]	376	340
	$4_1^+ \to 2_1^+$	728(3)	6.8(8)	589^{+79}_{-62}		521	507

TABLE VI. Absolute intrinsic quadrupole moments $|Q_0|$ and deformation parameters β_2 as extracted from experimental B(E2) values. Errors for β_2 are neglected due to its inherent approximative nature.

^{A}X	J_1^π	$|Q_0|(e\,\mathrm{fm}^2)$	$|\beta_2|$
^{58}Cr	2_1^+	107(7)	0.28
	4_1^+	88^{+7}_{-6}	0.22
	6_1^+	90^{+33}_{-20}	0.23
^{60}Cr	2_1^+	118^{+8}_{-6}	0.29
	4_1^+	123^{+12}_{-9}	0.31
	6_1^+	123^{+44}_{-22}	0.31
^{62}Cr	2_1^+	136^{+8}_{-6}	0.33
	4_1^+	144^{+9}_{-8}	0.35

its relative increase is comparable to the rapid increase of the $B(E2; 4_1^+ \to 2_1^+)$ value. Unfortunately, the large errors prevent a more quantitative discussion.

Before we proceed with the comparison of our data with the systematics, we briefly discuss the evolution of quadrupole moments and quadrupole deformation parameters. In the rotational model the (absolute) intrinsic quadrupole moment $|Q_0(J)|$ can be derived for $K \neq \frac{1}{2}, 1$ from the $B(E2; J \to J-2)$ value according to

$$B(E2; J \to J-2) = \frac{5}{16\pi}e^2 Q_0^2 |\langle JK20|J-2,K\rangle|^2. \quad (5)$$

The absolute intrinsic quadrupole moment $|Q_0|$ can be formulated—in first-order approximation and assuming a rigid rotor—as a function of the quadrupole deformation parameter β_2:

$$|Q_0| = \frac{3}{\sqrt{5\pi}}ZeR_0^2\beta_2, R_0 = 1.2A^{1/3}\,\mathrm{fm}. \quad (6)$$

The absolute $|Q_0|$ values and deformation parameters β_2 are shown in Table VI. Note that the calculated $|Q_0|$ for the 2_1^+ state in ^{58}Cr is significantly larger than the $|Q_0|$ for the 4_1^+ state. This indicates that the rotational limit is not applicable to describe the low-lying yrast structure in ^{58}Cr. This can also be deduced from ratios built from level energies of low-lying yrast states, which deviate significantly from the rotor limit. The experimental data indicate an increasing quadrupole deformation toward ^{62}Cr. The absolute intrinsic quadrupole moments for the 2_1^+ and 4_1^+ states both in ^{60}Cr and ^{62}Cr are comparable within the error, which is one of the characteristics of a rotorlike behavior. As expected, the steady increase in quadrupole collectivity toward $N = 40$ can also be seen in terms of the quadrupole deformation parameter β_2.

A. Qualitative discussion of the systematics

The systematic evolution of 2_1^+ state energies and corresponding reduced transition strengths $B(E2; 2_1^+ \to 0_1)^+$ are shown in Fig. 11 for Cr and neighboring isotopes, which include our new data.

For the neutron shell closure at $N = 28$, all depicted isotopes are characterized by high $E(2_1^+)$ and small $B(E2; 2_1^+ \to 0_1^+)$ values. For the harmonic oscillator shell
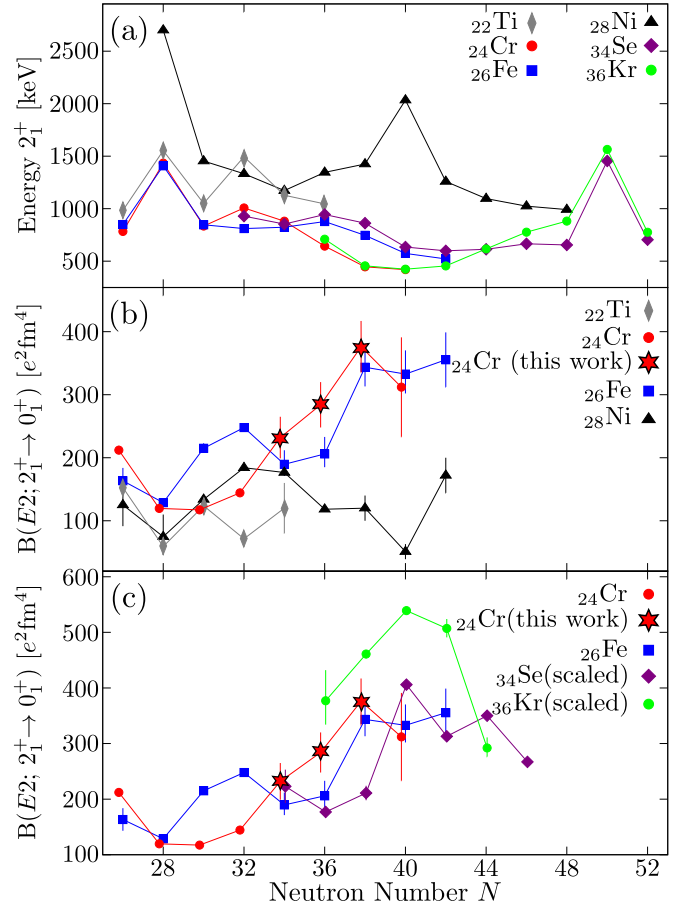

FIG. 11. (Color online) The evolution of first 2^+ state energies for $N = 26$–52 is shown in panel (a) and corresponding $B(E2)$ values are shown in panel (b). In panel (c) $B(E2)$ values of Fe and Cr are compared to the scaled $B(E2)$ values of their VPS partner Se and Kr, respectively. The scaling factor is given by $Z = (Z_L/Z_H)^2(A_L/A_H)$, where Z_H and A_H (Z_L and A_L) denote the atomic and mass numbers of the the heavier (lighter) partner. See Ref. [55] for details.

closure at $N = 40$, only ^{68}Ni exhibits signatures characteristic of a shell closure. However, as mentioned in the introduction, recent studies question this interpretation.

Compared to the Fe isotones, quadrupole collectivity evolves more rapidly along the Cr isotopes between $N = 34$ and $N = 38$. This can be understood qualitatively in terms of the attraction between the $\pi f_{7/2}$ orbital and the $\nu f_{5/2}$ orbital caused by the monopole part of the tensor force, whose strength correlates with the occupation of these orbitals. As a consequence, the gap between the single-particle energies of the $\nu f_{5/2}$ and the intruding $\nu g_{9/2}$ orbital is reduced in neutron-rich Cr compared to the Fe isotones [7,27].

The valence proton symmetry (VPS) [55] correlates reduced transition strengths $B(E2; 2_1^+ \to 0_1^+)$ in collective isotones with the same number of proton particles and holes with respect to a closed (sub)shell configuration. For neutron-rich Cr and Fe isotopes the VPS partners (Kr and Se) are chosen with respect to $Z = 30$ as was discussed in Ref. [17]. The trend of rapidly increasing quadrupole collectivity toward $N = 40$ can also be observed for the VPS partners. As expected in the

VPS, a significantly larger quadrupole collectivity is found for the Kr isotopes compared to the Se isotopes [see Fig. 11(c)].

Along the even-even Fe isotopes experimental $B(E2)$ values indicate a saturated quadrupole collectivity beginning at $N = 38$. For the Cr isotopes, our data suggest that the maximum in quadrupole collectivity is already reached at $N = 38$. However, the systematics are extended only up to one additional value at $N = 40$ and due to the relatively large errors a firm conclusion is not possible.

Approaching the less exotic nuclei with $N = 32$, a strikingly different behavior can be observed for the even-even isotones with $N = 32$ between $Z = 20$ and $Z = 28$. Both ^{54}Ti and ^{56}Cr exhibit a local rise in the 2_1^+ state energy and correspondingly small $B(E2)$ values. This sizable shell closure collapses completely in ^{58}Fe and ^{60}Ni. In fact, a crossing of the $B(E2)$ trends can be observed in Cr (Fe) when moving form $N = 32$ to $N = 34$.

A driving force behind the apparent phase change is the evolution of the $N = 32$ gap between the $\nu p_{3/2}$ orbital and the $\nu p_{1/2}$, $\nu f_{5/2}$ orbitals, which is distinctively smaller in the Fe-Ni nuclei compared to the Ti-Cr nuclei. This can be understood in terms of the spin-orbit splitting of the $\nu p_{1/2}$, $\nu p_{3/2}$ and the weakening effect of the $\pi f_{7/2}$ - $\nu f_{5/2}$ interaction with decreasing number of protons.

While $E(2_1^+)$ values and $B(E2; 2_1^+ \rightarrow 0_1^+)$ values are useful signatures to follow the evolution of quadrupole collectivity along an isotopic chain, the energy ratio $R_{42} = E(4_1^+)/E(2_1^+)$ and the transition strength ratio $B_{42} = B(E2; 4_1 \rightarrow 2_1^+)/B(E2; 2_1^+ \rightarrow 0_1^+)$ are helpful to classify structural properties. The R_{42} value is smaller than 2.0 for excited states dominated by single-particle excitation, equal to 2.0 for spherical vibrators and equal to 3.33 for a rigid rotor. Values around 2.5 are typically observed in (γ-soft) transitional nuclei.

The B_{42} value is 2.0 in the vibrator limit [56] and close to 1.43 in the rigid rotor limit [57]. A B_{42} value greater than 1.0 is a general feature shared by all collective models, whereas values close to one are usually observed in nuclei near shell closures in which the seniority is a good quantum number [58]. The B_{42} and R_{42} ratios are shown in Table VII for even-even Cr isotopes with $N \geqslant 28$.

Based on ratios between excitation energies of various excited states, ^{58}Cr was proposed [38] as a candidate for the

TABLE VII. Comparison of experimental $R_{4/2}$, $R_{6/2}$, $B_{4/2}$, and $B_{6/2}$ ratios for the even-even Cr isotopes with $N = 28$–38. In addition, the expected values in the $E(5)$ limit are shown.

	R_{42}	B_{42}	R_{62}	B_{62}
$E(5)$	2.20	1.68	3.59	2.21
^{52}Cr$_{28}$	1.65	$0.99^{+0.54}_{-0.26}$	2.17	0.51(2)
^{54}Cr$_{30}$	2.19	$2.00^{+0.43}_{-0.30}$	3.86	$1.23^{+0.48}_{-0.28}$
^{56}Cr$_{32}$	2.06	$1.29^{+0.06}_{-0.05}$	3.23	
^{58}Cr$_{34}$	2.20	$0.98^{+0.21}_{-0.18}$	3.66	$1.00^{+0.76}_{-0.34}$
^{60}Cr$_{36}$	2.27	$1.56^{+0.38}_{-0.29}$	3.89	$1.48^{+1.01}_{-0.50}$
^{62}Cr$_{38}$	2.64	$1.59^{+0.28}_{-0.23}$		

critical point of the shape phase transition from a vibrator to a γ-soft structure, known as the $E(5)$ dynamical symmetry proposed by Iachello [37]. The R_{42} value in ^{58}Cr matches the $E(5)$ signature perfectly and the $R_{62} = E(6_1^+)/E(2_1^+)$ ratio deviates only marginally. Our experimental B_{42} and B_{62} values, however, do not support the $E(5)$ assumption for ^{58}Cr. It is worth mentioning that a better agreement is found for ^{60}Cr: In addition to the R_{42} and R_{62} values supporting the $E(5)$ symmetry, both B_{42} and $B_{62} = B(E2; 6_1 \rightarrow 4_1^+)/B(E2; 2_1^+ \rightarrow 0_1^+)$ values are in good agreement with those expected in a nucleus at the critical point (see Table VII). It must be stressed that the $E(5)$ limit represents an ideal case and, as a consequence, slight deviations from these values are expected. The symmetry predicts specific values that involve nonyrast states. In particular, the position of the second 0^+ is relevant to further verify the underlying phase transitions. The best candidates for $E(5)$ phase transition identified so far, ^{128}Xe [59] and ^{134}Ba [60], lie in the valley of stability. In these cases, some nonyrast states have been observed and transition probabilities have been measured. On the other hand, ^{60}Cr constitutes the first nucleus far from stability hitherto identified as a good candidate for the $E(5)$ dynamical symmetry. The experimental limitations to populate nonyrast states in this nucleus and to measure the corresponding transition probabilities precludes at present the possibility of determining the position of the second 0^+ state.

B. Theoretical description

The experimental results are interpreted in the shell-model (SM) framework by means of large-scale calculations using the code ANTOINE [61] with the interaction LNPS [27], which is capable of reproducing with good accuracy experimental observables in the vicinity of $N = 40$; see, for instance, Refs. [18,62–65]. Indeed, recent studies in the neutron-rich even-even Fe isotopes [17,25] and Cr isotopes [23] showed that the inclusion of the neutron $0g_{9/2}$, $1d_{5/2}$ orbitals to the valence space is crucial to reproduce the experimentally observed rapid increase in quadrupole collectivity. The role of the neutron $1d_{5/2}$ orbital in this development was discussed in Ref. [24] and can be understood in terms of the quasi-SU(3) symmetry [66]. The SM calculations with the LNPS interaction are performed in an extended valence space in which the full pf shell is used for protons, while for neutrons the space spans over the $p_{3/2}$, $p_{1/2}$, $f_{5/2}$, $g_{9/2}$, $d_{5/2}$ orbitals [27]. In all calculations the effective charges deduced in Ref. [67] ($e_\pi = 1.31e$, $e_\nu = 0.46e$) are used. The theoretical results are compared to the experimental findings in Fig. 12. The LNPS calculations reproduce very well the low-lying level schemes toward $N = 40$. Beginning at $N = 34$, the calculations predict rapidly and almost linearly increasing $B(E2; 2_1^+ \rightarrow 0_1^+)$ values toward $N = 38$. Lenzi *et al.* [27] predict a transition toward a strongly deformed prolate shape at $N = 40$ which is reflected in the enhanced $B(E2)$ values for higher-lying transitions.

Our results for the lowest yrast transitions are in very good agreement with the calculations within the experimental uncertainties. The experimental $B(E2)$ values, however, indicate
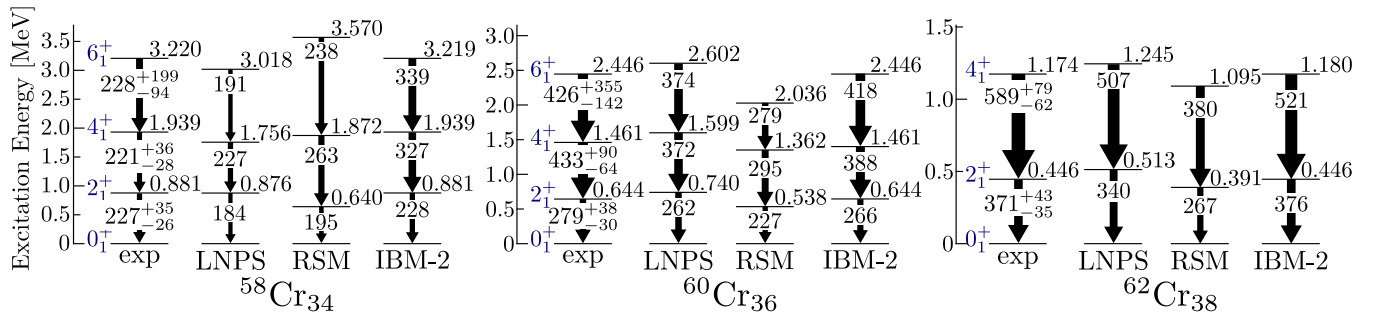
FIG. 12. (Color online) Comparison of excitation energies (in MeV) and $B(E2)$ values in ^{58,60,62}Cr with SM calculations using the interaction LNPS [27], realistic SM calculations [31], and IBM-2 calculations [27]. Values on arrows indicate the $B(E2)$ values in units of e^2fm^4. The thickness of the arrows is proportional to the corresponding $B(E2)$ value. See text for details.

a trend toward a more collective behavior compared to the calculations.

The occupation numbers of the most relevant neutron and proton orbitals as obtained by the SM calculations are plotted in Fig. 13 for the ground states in ^{58,60,62}Cr. In ^{58}Cr the contributions of the $\nu g_{9/2}$ and $\nu d_{5/2}$ orbitals to the wave function are only marginal. When approaching $N = 40$ the occupation of these orbitals increases, which gives rise to the onset of collectivity. This is accompanied by the decrease of the occupation of the proton $f_{7/2}$ orbital in favor of the increasing occupation of the proton $p_{3/2}$ and $f_{5/2}$ orbitals.

Recently, a new effective interaction has been derived by Coraggio *et al.* [31,68] from a low-momentum potential, using the realistic CD-Bonn nucleon-nucleon potential. Figure 12 reports the results obtained with this realistic shell-model calculations (RSM) for ^{58,60,62}Cr. These calculations are performed in a model space which consists of $f_{7/2}$, $p_{3/2}$ for protons and $p_{3/2}$, $p_{1/2}$, $f_{5/2}$, $g_{9/2}$, $d_{5/2}$ for neutrons.

While the excitation energies are well reproduced, the RSM calculations underestimate the rapid increase of the $B(E2)$ values between $N = 34$ and $N = 38$, indicating a lack of collectivity of the calculated states.
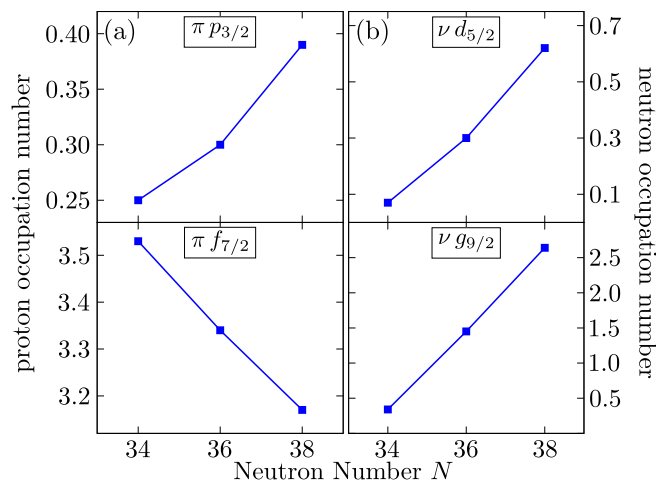

FIG. 13. (Color online) Occupation numbers in the wave functions of the ground states in ^{58,60,62}Cr as calculated with the LNPS interaction. (a) Results for the proton $p_{3/2}$ and $f_{7/2}$ orbitals. (b) Results for the neutron $d_{5/2}$ and $g_{9/2}$ orbitals.

Finally, we compare our results with phenomenological IBM-2 calculations as recently published in Ref. [32], which offer a simple framework to investigate collective properties. Due to the underlying fitting procedure of the parameters [32], IBM-2 calculations reproduce the energies of low-lying yrast states and the experimental $B(E2; 2_1^+ \rightarrow 0^+)$ values very well. The calculated $B(E2)$ values for higher-lying transitions reproduce the data within the experimental uncertainties. The calculated $B(E2; 4_1^+ \rightarrow 2_1^+)$ value in ^{58}Cr features the only exception, which is close to the expected value in the rigid rotor limit but deviates significantly from the experimental value.

We conclude our discussion with a short remark on the evolution of quadrupole collectivity toward ^{64}Cr with $N = 40$. Based on 2_1^+ state energies and $B(E2; 2_1^+ \rightarrow 0_1^+)$ values the theoretical approaches predict that a saturation of quadrupole collectivity in Cr begins at $N = 38$. This is consistent with experimental information on the excitation energies of the 2_1^+ state in ^{62}Cr and ^{64}Cr [16]. Our $B(E2; 2_1^+ \rightarrow 0_1^+)$ in ^{62}Cr is in agreement with the corresponding value in ^{64}Cr as measured by Crawford and coworkers [18].

Although this supports the observation of a saturated collectivity at $N = 38$, the large errors for the transition strengths do not allow a firm conclusion.

V. CONCLUSIONS

In summary, the excited states in ^{58,60,62}Cr were populated in one-proton knockout reactions and corresponding level lifetimes were measured with the recoil distance Doppler-shift technique. This constitutes the first systematic study of transition probabilities for the yrast 2_1^+, 4_1^+, and 6_1^+ states in the new deformed region of neutron-rich Cr isotopes around $N = 40$. The results show a rapid transition from a spherical vibrator to deformed rotor behavior, with ^{60}Cr as a potential candidate for the critical point of the $E(5)$ dynamical symmetry. The experimental findings have been compared to IBM-2 and shell-model calculations using different effective interactions and model spaces. While all calculations describe the data fairly well, the shell-model calculations using the largest model space and the LNPS interaction best reproduce the evolution of the collectivity toward $N = 40$.

[1] C. Détraz *et al.*, Phys. Rev. C **19**, 164 (1979).
[2] T. Motobayashi *et al.*, Phys. Lett. B **346**, 9 (1995).
[3] C. R. Hoffman *et al.*, Phys. Lett. B **672**, 17 (2009).
[4] R. Kanungo *et al.*, Phys. Rev. Lett. **102**, 152501 (2009).
[5] A. N. Andreyev *et al.*, Nature (London) **405**, 430 (2000).
[6] T. Otsuka, R. Fujimoto, Y. Utsuno, B. A. Brown, M. Honma, and T. Mizusaki, Phys. Rev. Lett. **87**, 082502 (2001).
[7] T. Otsuka, T. Suzuki, R. Fujimoto, H. Grawe, and Y. Akaishi, Phys. Rev. Lett. **95**, 232502 (2005).
[8] T. Otsuka, T. Suzuki, M. Honma, Y. Utsuno, N. Tsunoda, K. Tsukiyama, and M. Hjorth-Jensen, Phys. Rev. Lett. **104**, 012501 (2010).
[9] S. K. Patra and C. R. Praharaj, Phys. Rev. C **47**, 2978 (1993).
[10] R. Broda *et al.*, Phys. Rev. Lett. **74**, 868 (1995).
[11] O. Sorlin *et al.*, Phys. Rev. Lett. **88**, 092501 (2002).
[12] N. Bree *et al.*, Phys. Rev. C **78**, 047301 (2008).
[13] C. Guénaut *et al.*, Phys. Rev. C **75**, 044303 (2007).
[14] K. Langanke, J. Terasaki, F. Nowacki, D. J. Dean, and W. Nazarewicz, Phys. Rev. C **67**, 044314 (2003).
[15] S. N. Liddick *et al.*, Phys. Rev. C **87**, 014325 (2013).
[16] A. Gade *et al.*, Phys. Rev. C **81**, 051304 (2010).
[17] W. Rother *et al.*, Phys. Rev. Lett. **106**, 022502 (2011).
[18] H. L. Crawford *et al.*, Phys. Rev. Lett. **110**, 242701 (2013).
[19] S. Zhu *et al.*, Phys. Rev. C **74**, 064315 (2006).
[20] O. Sorlin *et al.*, Eur. Phys. J. A **16**, 55 (2003).
[21] N. Aoi *et al.*, Phys. Rev. Lett. **102**, 012502 (2009).
[22] M. Seidlitz *et al.*, Phys. Rev. C **84**, 034318 (2011).
[23] T. Baugher *et al.*, Phys. Rev. C **86**, 011305 (2012).
[24] E. Caurier *et al.*, Eur. Phys. J. A **15**, 145 (2002).
[25] S. Lunardi *et al.*, Phys. Rev. C **76**, 034303 (2007).
[26] K. Kaneko, Y. Sun, M. Hasegawa, and T. Mizusaki, Phys. Rev. C **78**, 064312 (2008).
[27] S. M. Lenzi, F. Nowacki, A. Poves, and K. Sieja, Phys. Rev. C **82**, 054301 (2010).
[28] H. Oba and M. Matsuo, Progr. Theor. Phys. **120**, 143 (2008).
[29] L. Gaudefroy *et al.*, Phys. Rev. C **80**, 064313 (2009).
[30] K. Sato, N. Hinohara, K. Yoshida, T. Nakatsukasa, M. Matsuo, and K. Matsuyanagi, Phys. Rev. C **86**, 024316 (2012).
[31] L. Coraggio, A. Covello, A. Gargano, and N. Itaco, Phys. Rev. C **89**, 024319 (2014).
[32] J. Kotila and S. M. Lenzi, Phys. Rev. C **89**, 064304 (2014).
[33] F. Iachello, Int. J. Mod Phys B **20**, 2687 (2006).
[34] P. Cejnar *et al.*, Rev. Mod. Phys. **82**, 2155 (2010).
[35] M. P. Carpenter, R. V. F. Janssens, and S. Zhu, Phys. Rev. C **87**, 041305 (2013).

[36] N. Mărginean *et al.*, Phys. Lett. B **633**, 696 (2006).
[37] F. Iachello, Phys. Rev. Lett. **85**, 3580 (2000).
[38] F. Marti *et al.*, in *Proceedings of the 2001 Particle Accelerator Conference, PAC 2001*, Vol. 4 (IEEE, Piscataway, NJ, USA, 2001), pp. 2557–2559.
[39] D. J. Morrissey *et al.*, Nucl. Instr. Meth. Phys. Res. B **204**, 90 (2003).
[40] D. Bazin *et al.*, Nucl. Instr. Meth. Phys. Res. B **204**, 629 (2003).
[41] A. Dewald *et al.*, Prog. Part. Nucl. Phys. **67**, 786 (2012).
[42] H. Iwasaki *et al.* (unpublished).
[43] H. Iwasaki *et al.*, Phys. Rev. Lett. **112**, 142502 (2014).
[44] A. Nichols *et al.*, Phys. Lett. B **733**, 52 (2014).
[45] J. Yurkon *et al.*, Nucl. Instr. Meth. Phys. Res. A **422**, 291 (1999).
[46] Y. Fuchi *et al.*, in *Conference Record of the 1992 IEEE Nuclear Science Symposium and Medical Image Conference*, Vol. 1 (IEEE, Piscataway, NJ, USA, 1992), pp. 172–174.
[47] W. F. Mueller *et al.*, Nucl. Instr. Meth. Phys. Res. A **466**, 492 (2001).
[48] K. Makino and M. Berz, Nucl. Instr. Meth. Phys. Res. A **558**, 346 (2006).
[49] T. K. Alexander and A. Bell, Nucl. Instr. Meth. **81**, 22 (1970).
[50] P. Adrich *et al.*, Nucl. Instr. Meth. Phys. Res. A **598**, 454 (2009).
[51] A. Lemasson *et al.*, Phys. Rev. C **85**, 041303 (2012).
[52] R. Brun and F. Rademakers, Nucl. Instr. Meth. Phys. Res. A **389**, 81 (1997).
[53] S. Agostinelli *et al.*, Nucl. Instr. Meth. Phys. Res. A **506**, 250 (2003).
[54] A. Bürger *et al.*, Phys. Lett. B **622**, 29 (2005).
[55] A. Dewald *et al.*, Phys. Rev. C **78**, 051302 (2008).
[56] G. Gneuss and W. Greiner, Nucl. Phys. A **171**, 449 (1971).
[57] A. S. Davydov and G. F. Filippov, Nucl. Phys. **8**, 237 (1958).
[58] J. Ressler *et al.*, Phys. Rev. C **69**, 034317 (2004).
[59] R. M. Clark *et al.*, Phys. Rev. C **69**, 064322 (2004).
[60] R. F. Casten and N. V. Zamfir, Phys. Rev. Lett. **85**, 3584 (2000).
[61] E. Caurier and F. Nowacki, Act. Phys. Pol. B **30**, 705 (1999).
[62] A. Gade *et al.*, Phys. Rev. Lett. **112**, 112503 (2014).
[63] C. Louchart *et al.*, Phys. Rev. C **87**, 054302 (2013).
[64] F. Recchia *et al.*, Phys. Rev. C **85**, 064305 (2012).
[65] F. Recchia *et al.*, Phys. Rev. C **88**, 041302 (2013).
[66] A. P. Zuker, J. Retamosa, A. Poves, and E. Caurier, Phys. Rev. C **52**, R1741(R) (1995).
[67] M. Dufour and A. P. Zuker, Phys. Rev. C **54**, 1641 (1996).
[68] L. Coraggio (private communication).